Optimization of Extension-Twist Coupled Composite Blades for High-Speed Rotorcraft

Matthew DiPalma
PhD. Student

Etana Ferede
Research Scientist

Farhan Gandhi
Redfern Chair in Aerospace Engineering

Center for Mobility with Vertical Lift
Rensselaer Polytechnic Institute
Troy, NY 12180

ABSTRACT

A variable stiffness composite optimization methodology is presented to study the extension-twist coupling capability of composite rotor blades to passively vary the elastic twist distribution as a function of the rotational speed of the rotor. To this end, an optimization framework, with composite laminates as design variables, is implemented to optimize an extension-torsion-coupled composite blade based on the UH-60A Black Hawk. The results show that variation in twist angle of up to 9° can be achieved by reducing the rotor speed by 20% (from 100%NR to 80%NR) using optimized composite laminates while complying with material strength constraints under both centrifugal and aerodynamic loads in hover. Using this optimized design, a composite blade could be constructed with 13° nose-up structural twist. As the rotor is spun up to 100%NR (for hover), the blade elastically twists nose-down to a near-optimum linear twist distribution of −12.5°. Yet when the rotor speed is reduced to 80%NR to potentially accommodate compressibility effects on the advancing blade tip in high-speed forward flight, the blade elastically untwists to only −3.5° of linear tip twist along the blade span. This passive twist adaptivity could improve a wide range of rotor performance metrics, including power, hub vibrations, and root bending loads, across both flight regimes.

INTRODUCTION

Conventional helicopter rotor blades typically have a large negative twist variation from root to tip to minimize induced power in hover and low-speed operation. However, this washout is highly detrimental to operation in high-speed flight, increasing both sectional aerodynamic drag, as well as generating negative lift on the advancing blade tip of an edgewise rotor. Previous studies on various rotors (Refs. 1, 2) have shown that a twisted blade in forward flight increases n/rev vibratory loads by over 100%, flap bending moments by over 32%, and power-requirements by over 5%. For tilt-rotor aircraft the situation is reversed, with the ideal propeller twist (for operation at high speed in axial flow conditions) being significantly greater than the twist required of a hovering rotor. For both cases, though, the ability to change blade twist distribution between hover and high-speed cruise could significantly improve performance over diverse segments of the flight regime.

Previous efforts to change blade twist with flight condition have fallen under two categories. The first uses actuation to induce change in blade twist, with the ONR/Boeing Reconfigurable Rotor Blade program being an example. This program used Shape Memory Alloy (SMA) torque tube actuators to twist a scaled V-22 Osprey blade (Refs. 3–6). However, due to the high baseline rotor stiffness the twist generated was very modest (of the order of a couple of degrees) despite the large moment production capability of the SMA actuators. Another example (Ref. 7) used skin warping to generate significant twist, but this morphing blade design had an inherently reduced torsion stiffness.

The second category eschews the use of powered actuators on the rotor blades, exploiting instead the change in centrifugal force with change in rotor RPM to produce twist changes on rotor blades with extension-twist coupling. Researchers have also previously used change in CF force to produce changes in rotor blade span and chord (Refs. 8, 9). The idea of using change in CF force to produce change in twist is potentially very attractive for high-speed rotorcraft (tilt-rotor aircraft, slowed-rotor compound aircraft, and coaxial-rotor aircraft) where it is routine for the rotors to undergo an RPM reduction in high-speed flight. In the late 1980s through early 1990s, scientists at the US Army Research Lab (at Langley Research Center) devoted much effort to the design of extension-twist coupled composite rotor blades (Refs. 10–12).

Presented at the AHS International 74rd Annual Forum & Technology Display, Phoenix, Arizona, USA, May 14–17, 2018.

However, only modest change in blade twist was achieved going between the rotational speeds corresponding to hover and high-speed cruise. Furthermore, ballast weight introduced to increase twist change resulted in a mass penalty on the blades. The use of Flexible Matrix Composites for extension-twist coupled rotors has been proposed (Refs. 13, 14). While a larger twist per unit axial load could be achieved, the torsional stiffness of the blade becomes unacceptably low. Recently, Ward et al. (Refs. 15–17) parametrically varied the ply layups of a box-beam spar used as a structural proxy for a UH-60A Black Hawk rotor blade to realize extension-twist couplings that produce changes in tip twist as a result of changes in rotor RPM between hover and high-speed flight. While twist changes as high as 4-10° were predicted in the absence of any failure considerations, imposing material strain limits reduced the achievable twist to around 1°.

From the above studies, it is clear that achieving appreciable twist variation through RPM variation in an extension-twist coupled rotor blade without violating material strain or blade stiffness constraints remains a challenge. Many of the studies have used simplified box-beam type representations of the blade spar (rather than modeling the entire blade cross-section), considered only uniform layups along the span, and a parametric variation in composite ply angles.

The present study seeks to advance these prior design efforts by modeling the entire rotor blade cross-section (instead of a box-beam or some simplified representation), allowing both chord-wise and span-wise variation of the composite laminates, and using optimization methods to maximize the achievable twist change in an extension-twist coupled blade while imposing failure constraints appropriate for composite structures.

METHODOLOGY/OPTIMIZATION SETUP

The optimization framework presented here is intended for optimizing extension-torsion coupled composite rotor blades based on the UH-60A Black Hawk rotor. The rotor blades considered in this study use the airfoil geometries and planform specifications of the UH-60A Black Hawk blade, matching its stiffness, but do not consider the large nose-down geometric twist of the Black Hawk blade (using untwisted geometry instead as a point of departure). A gradient-based optimization process is used to design the optimal extension-torsion coupled blade, using the optimization set-up depicted in Figure 1. The optimization process shown in Figure 1 is as follows: starting from the initial (material) design variables and rotor specifications (rotor diameter, span-wise distribution of chord, twist, and local blade axis), the blade geometry and its material properties are generated based on the IsoGeometric Analysis (IGA) principle. IGA is a computational approach that unifies finite element analysis with a NURBS-based Computer Aided Design (CAD) method (Ref. 18). Non-Uniform Rational B-Spline (NURBS) representations are commonly used to construct descriptions of engineering products. Next, the tip twist in vacuum is calculated, for a given centrifugal load, using a nonlinear beam model that uses sectional stiffness constants of a composite beam (Ref. 19). The (beam) stiffness constants are calculated using a sectional analysis model for thin-walled, multi-cell, composite beams (Ref. 20). Next, the centrifugal loads, calculated using the reduced order model, are applied as static load on a full finite element representation of the blade and the stress response to centrifugal load is calculated. The stress responses are used to formulate the material constraints based on a conservative failure envelope which is similar to the Tsai-Wu failure criteria for composite materials (Ref. 21). The tip twist, material failure constraint, and constraints on the beam stiffness properties, together with their respective sensitivities to the design variables, are passed to '`fmincon`' (`MATLAB`-based optimizer), which iterates over the design variables to maximize the objective while satisfying all the constraints.

The definition of a rotor blade geometry and material property follows the methodology presented in Figure 2, where a multi-level discretization scheme is used to parametrize the beam axis, chord, twist, and material distribution using successively finer control point nets. The mapping between different levels of refinement is performed using the Knot refinement method (Ref. 22). Referring to Figure 2, the beam axis is described as a 3D NURBS curve with the corresponding control points locations defined on the L_1 level. On the L_2 level, the cross-section variation (along the blade span) is parametrized by associating an airfoil geometry with each control point and interpolating using NURBS functions. The airfoil geometry associated with each control point is generated by a linear combination of predefined airfoil shapes. The orientation of each airfoil is defined by the local twist, which is also represented by a NURBS function and control point nets on the L_2 level. Composite laminates are used to define the material properties of a rotor blade. The laminate properties are described by a NURBS curve with the corresponding control point properties defined on the L_3 level (see Figure 2). The laminate properties per control point are determined by dividing a cross-section in $N_{pr}+1$ sections, where N_{pr} laminates are assigned over the contour of a cross-section and a single laminate for the shear webs. Extension-torsion coupling is caused by antisymmetric layup, where the orientation of the layup on the top and bottom of the airfoil is the same but with reversed sign. Therefore, N_{pr} refers to the number of laminates over the airfoil chord. A schematic representation of laminate assignment per cross-section is shown in Figure 3, where for the current study, 4 laminates are used to define the material properties over a cross-section ($N_{pr}=3$). Symmetric laminates are used in the current optimization studies. Hence, the coupling matrix (B) is zero for all laminates considered. Furthermore, the first and second shear webs are located respectively at $0.35c$ and $0.7c$, where c is the chord length.

The parameterization of a single laminate is shown in Figure 4. The design variables per laminate are: laminate thickness h, off-axis fiber angle θ, and thickness ratio of the off-axis fiber e. In this study, "off-axis fiber" refers to the fibers located in the top and bottom layers of Figure 4, which in general are not oriented along the blade axis. The mid-section of the laminate consists of a quasi-isotropic layup which cannot vary. This

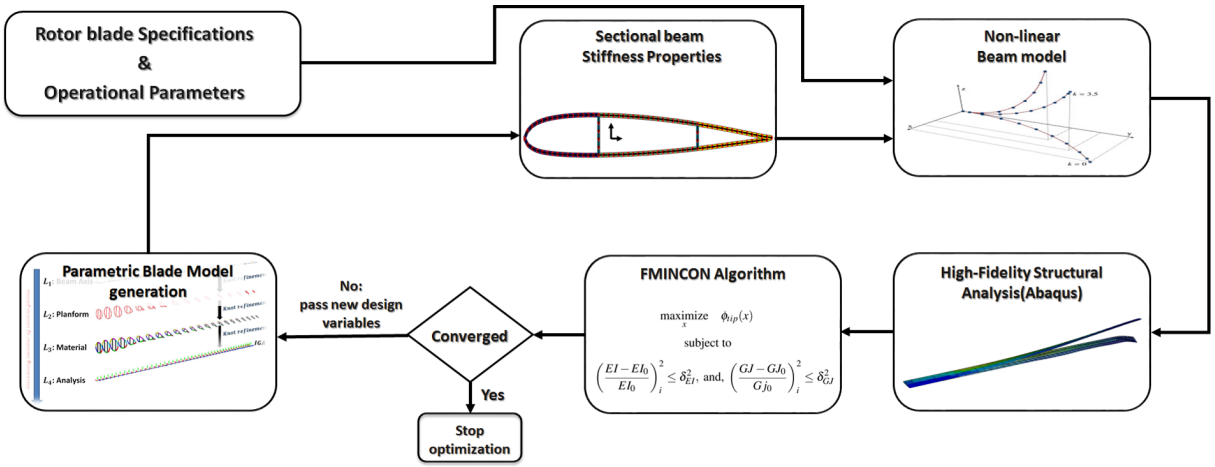

Fig. 1. Schematic overview of the optimization methodology.

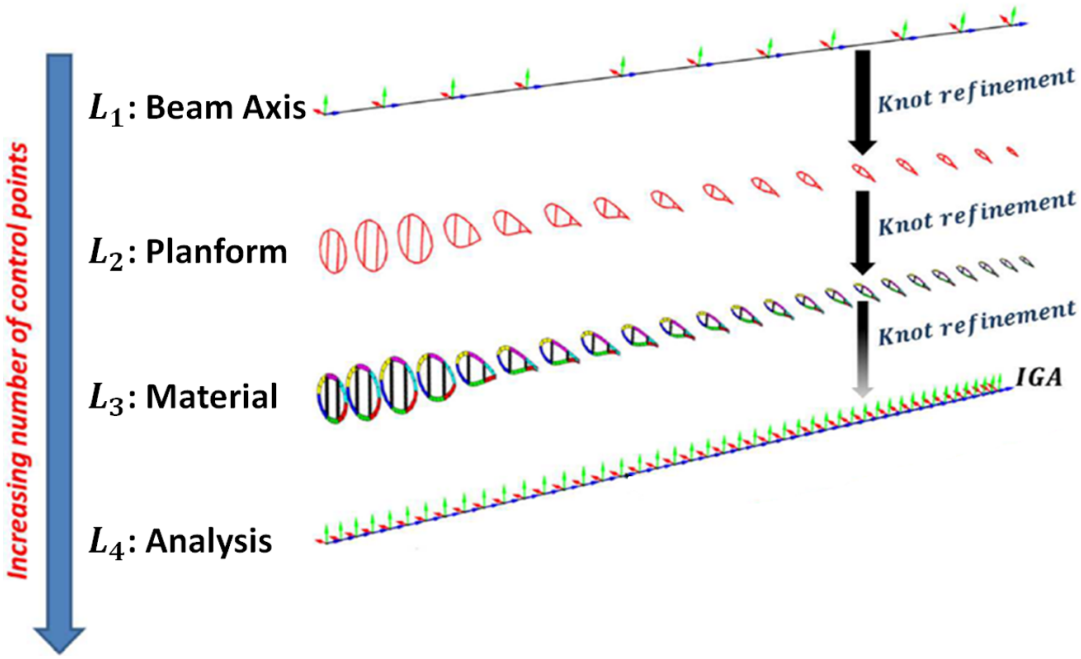

Fig. 2. Multi level parametrization of a rotor blade.

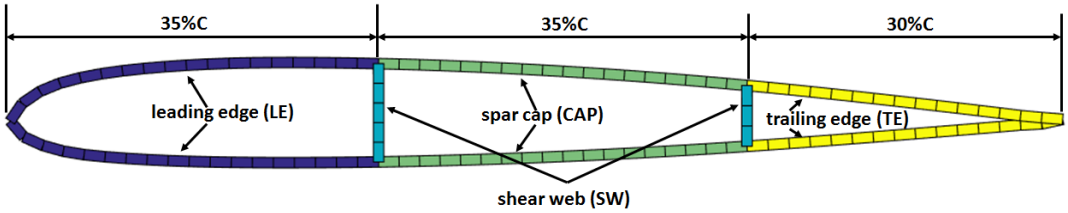

Fig. 3. Material property assignment over a cross-section, where each color represents a single laminate.

results in three design variables per laminate.

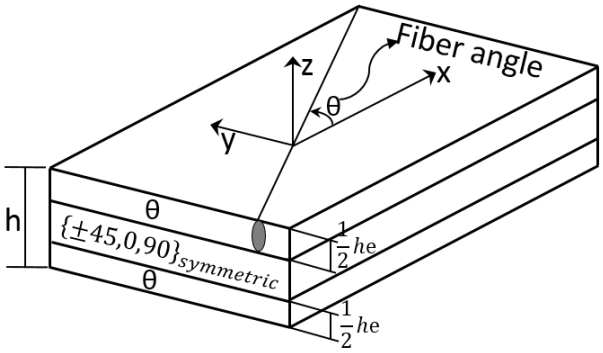

Fig. 4. Parametrization of a single laminate.

MATERIAL FAILURE CRITERIA

The present optimization features material failure criteria as a constraint. A conservative failure envelope, which is valid for any ply orientation, is implemented to check for material failure. The method is based on the Tsai-Wu failure criterion, modified to guarantee no material failure occurs in the laminate irrespective of the ply angle (Ref. 21). A failure index, defined as the ratio between the calculated strains and the corresponding strains on the failure envelope, is formulated such that a failure index larger than one indicates material failure. The failure index is written in terms of the average membrane strain of element i as:

$$r_i = \frac{1}{2}F_1 I_1 + \sqrt{\frac{1}{2}\sqrt{(0.5F_1^2 + (F_{11}+F_{12}))I_1^2 + (F_{11}-F_{12})I_2}}, \tag{1}$$

where:

$$I_1 = \varepsilon_x^i + \varepsilon_y^i,\ I_2 = \frac{1}{4}(\varepsilon_x^i - \varepsilon_y^i)^2 + (\gamma_{xy}^i)^2. \tag{2}$$

The strength tensors F_i and F_{ij}, that define the conservative failure envelope, are derived from the laminate failure strain limits: ε_{tens}, ε_{comp}, and γ_{shear}. The membrane strains of element i are calculated from the membrane stress components, averaged over the laminate thickness, as:

$$\begin{Bmatrix} \varepsilon_x^i \\ \varepsilon_y^i \\ \gamma_{xy}^i \end{Bmatrix} = A_i^{-1} \begin{Bmatrix} N_x^i \\ N_y^i \\ N_{xy}^i \end{Bmatrix}, \tag{3}$$

where A_i is the membrane stiffness of element i, while the average membrane stress components $N_i = \{N_x \quad N_y \quad N_{xy}\}_i^t$ are given by:

$$N_i = \frac{1}{2}h_i(\sigma_i^u + \sigma_i^l), \tag{4}$$

with the super scripts $()^u$ and $()^l$ denoting the membrane stress components at the upper and lower surface of element i with a thickness of h_i.

A finite element model of the UH-60A rotor blade is created using the FEA software ABAQUS, version 6.13. The model consists of 900 quadrilateral shell elements with reduced integration (S4R). Static linear analysis is performed where the centrifugal load is applied as static load obtained from the static analysis using the non-linear beam model (see Fig 1).

BASELINE DESIGN INCLUDING CENTRIFUGAL LOAD

A composite blade based on the UH-60A articulated rotor blade is used to investigate the extension-torsion coupling capability of composite laminates to vary the elastic twist of the rotor blade as a function of the centrifugal load. The elastic twist is the rotation of the blade with respect to the beam axis due to the centrifugal load or an external applied load, where the beam axis is along the blade span. A baseline blade is determined with similar geometric properties of the UH-60A Black Hawk, except for the structural twist, which is set to zero. Key geometric and operational properties of the UH-60A-like baseline blade are summarized in Table 1. The stiffness properties of the baseline design are obtained by

Table 1. Key properties of the UH-60A-like blade.

Parameters	
Rotor radius (m)	8.17
Blade chord (m)	0.53
Rotor speed (rpm)	258
Untwisted rotor blade	

matching the flap-wise bending, torsion, and average of the axial extensional stiffness to the corresponding stiffness components of the original UH-60A rotor blade. The average of the extensional stiffness (as opposed to the span-wise distribution itself) is taken as a metric of comparison between the blade designs because the established and accepted Rotorcraft Comprehensive Analysis System (RCAS) implementation of the UH-60A rotor blade features a span-wise constant axial stiffness. Furthermore, material failure constraint is considered in the optimization formulation, such that the final design does not fail under centrifugal load.

Due to the high stiffness to weight ratio of carbon fiber composites, it is found that the composite design results in significantly lower blade mass compared to the original UH-60A rotor blade, where the D-spar is constructed from titanium. Naturally, this reduction in the blade mass distribution substantially reduces the centrifugal load, which is the source of passive actuation for extension-torsion coupling. In this study, supplemental distributed mass is introduced so that the blade mass distribution is equal to that of the original UH-60A blade. This results in the generation of sufficient centrifugal load for passive twist actuation. A similar approach was implemented in previous studies (Refs. 15–17).

A baseline blade design is obtained through an optimization routine that minimizes the difference in aforementioned stiffness components, where the design variables are the laminate thickness (h) and thickness ratio of the off-axis fiber (e). The

Table 2. Single ply material properties for carbon fiber composite. (Ref. 17)

E_{11},GPa	E_{22},GPa	G_{12},GPa	ν	ρ,Kg/m^3
142	**9.79**	**5.93**	**0.42**	**1580**
Strain allowables				
$\varepsilon_{tension}\%$	$\varepsilon_{compresion}\%$		$\gamma_{shear}\%$	
0.6	**0.77**		**0.65**	

angle of the off-axis fiber angle (θ) is set to zero (aligned with the beam axis) for all laminates except those associated with the shear webs, where the off-axis fiber angle (θ) is set to -45° to accommodate shear. The material properties of the composite laminates are presented in Table 2. Four laminates constitute a cross-section (per control point), and 26 control points are distributed along the blade span, which amounts to 104 laminates and 208 design variables. The optimizer starts from an initial thickness of 10mm and a thickness ratio of 0.1 for all laminates considered.

Figure 5 compares the optimized torsional (GJ), flap-wise bending ($EI-flap$), extension (EA), and lag-wise bending ($EI-lag$) stiffness distributions of the baseline design with the corresponding stiffness properties of the UH-60A rotor blade, as implemented in the RCAS model. The average difference between the new baseline design and the RCAS model for GJ is 2%, for EA is 11%, for $EI-flap$ is 5%, and for $EI-lag$ is substantial (because the optimizer does not consider constraints on this stiffness component). Incorporating the lag-wise bending stiffness as part of the objective would result in severely sub-optimal designs across all the stiffness components, as the current limited and simplified parameterization cannot accommodate closely matching the complete set of stiffness distributions. The stiffness distribution of the new design is, in general, higher when compared against the stiffness components of the original RCAS model. This is the result of adding the material failure constraint as part of the optimization formulation which increases the laminate thickness in order to reduce local strains and comply with the failure constraint.

Figure 6 shows the design solutions corresponding to the stiffness results of Figure 5. The captions in Figure 6 refer to the span-wise variation of the: leading edge (LE), spar cap (CAP), trailing edge (TE), and shear web (SW) laminates (see Figure 3). The design shows large laminate thickness towards the blade root, especially for the shear webs and leading edge laminates, to match the large torsional and flap-wise bending stiffness of the RCAS model of the UH-60A blade, while complying with material strength constraints. It is also observed that the shear web laminates have substantial thickness ratios exceeding 0.5 along the blade span. This suggests that a large percentage of those laminates are composed of the off axis-fiber angles (see Figure 4).

Finally, it is observed from Figure 7 that the material failure index is less than one throughout the structure, indicating the blade has not failed with regards to material constraints under pure centrifugal loading at 100%NR.

EFFECT OF STIFFNESS CONSTRAINT ON TIP TWIST

Starting from the initial stiffness properties (Fig 5) of the baseline design (Fig 6), several optimizations are carried out to maximize the elastic twist at the blade tip while introducing constraints on the stiffness properties of the new designs. In the current study, a positive elastic twist results in nose-down rotation of the blade, which is desirable for the present application. The design variables (x) are chord-wise and span-wise variation of laminate thickness (h) and thickness ratio (e) together with chord-wise variation of fiber angle (θ), such that:

$$\begin{aligned} \underset{x}{\text{maximize}} \quad & \phi_{tip}(x) \\ \text{subject to:} \quad & max\left(\left|\frac{EI-EI_0}{EI_0}\right|\right) \leq \delta_{EI}, \\ & max\left(\left|\frac{GJ-GJ_0}{GJ_0}\right|\right) \leq \delta_{GJ}, \end{aligned} \tag{5}$$

where ϕ_{tip} is the elastic twist at the blade tip, while EI and GJ are, respectively, span-wise variation of the flap-wise bending and torsional stiffness. The variables δ_{EI} and δ_{GJ} are change of the stiffness constants relative to the baseline flap-wise bending (EI_0) and torsional (GJ_0) stiffness values at any span-wise station. The operator $max()$ refers to the maximum value of the argument. Four laminates define the material properties within a cross-section (per control point), with 26 control points along the blade span. The variables per laminate consist of laminate thickness (h), thickness ratio (e), and fiber angle (θ). For a full chord-wise and span-wise discretization of the 3 types of design variables, 316 total design variables would be required. However, as the off-axis fiber angle is taken to be constant along the span-wise coordinate, the vector x contains only 212 design variables.

Figure 8 depicts a contour plot of the elastic twist at the blade tip (ϕ_{tip}), evaluated at 100% the nominal rotation rate. The two axes δ_{EI} and δ_{GJ} represent changes in the stiffness constants relative to the baseline flap-wise bending (EI_0) and torsional (GJ_0) stiffness, respectively. Referring to Figure 8, the elastic twist seems to be more sensitive to change in flap-wise bending stiffness (δ_{EI}) than torsional stiffness (δ_{GJ}). A significant reduction in elastic tip twist is observed for more stringent constraint on δ_{EI}, 12° being the smallest elastic tip twist for δ_{EI} less than 15% and across the entire range of δ_{GJ}. Realizing a large elastic tip twist of up to 30° requires a reduction in flap-wise stiffness of as much as 35%.

MAXIMIZE ELASTIC TWIST UNDER CENTRIFUGAL LOAD

Several optimizations are carried out to maximize the elastic twist at the blade tip while introducing constraints on the flap-wise bending stiffness, torsional stiffness, and average of extensional stiffness (relative to the baseline design), together with material failure constraint. The design variables (x) are chord-wise and span-wise variation of laminate thickness (h)

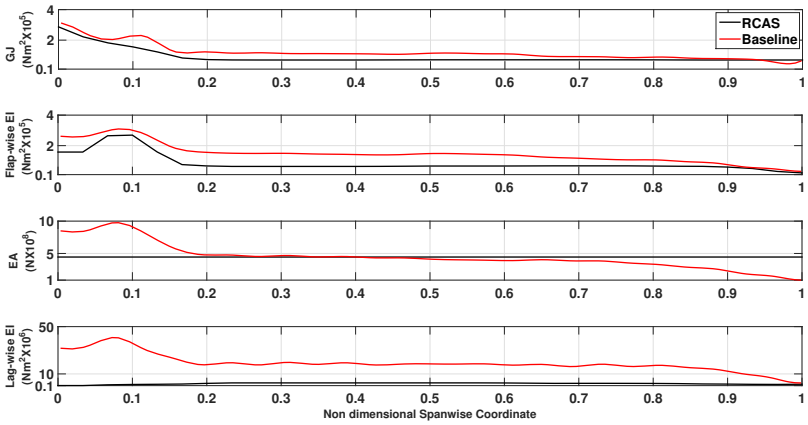

Fig. 5. Stiffness comparison for baseline design.

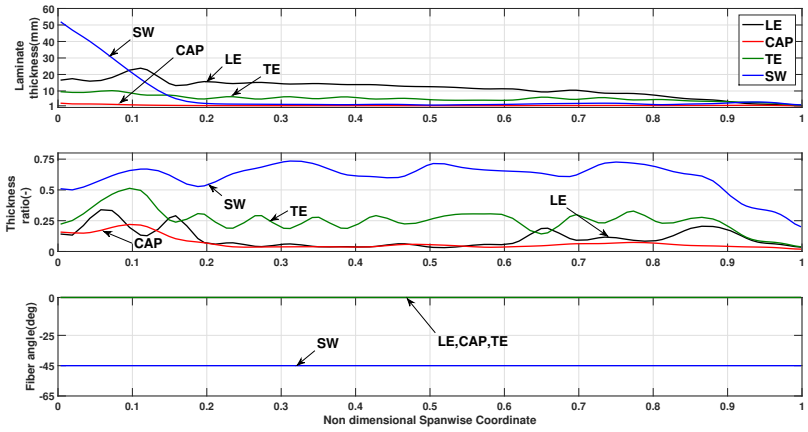

Fig. 6. Design solution for baseline design.

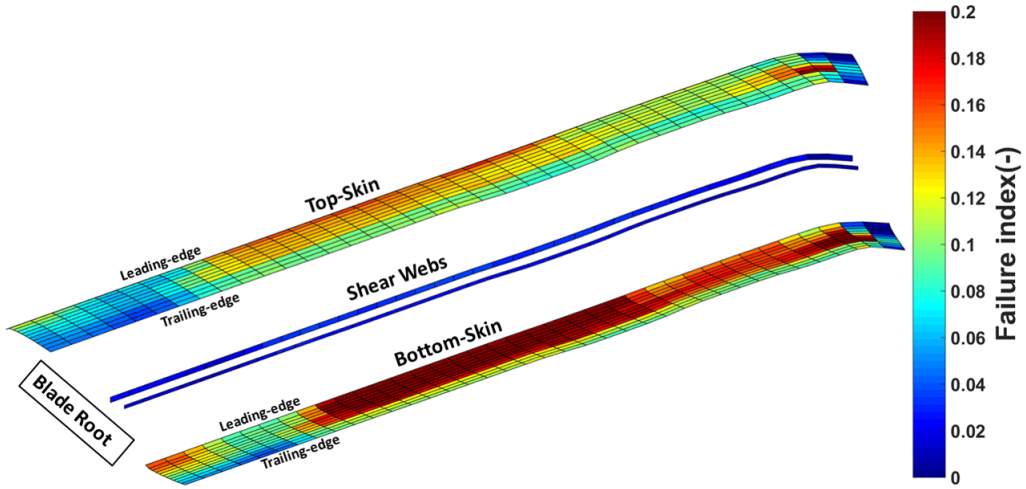

Fig. 7. Material failure index for baseline design.

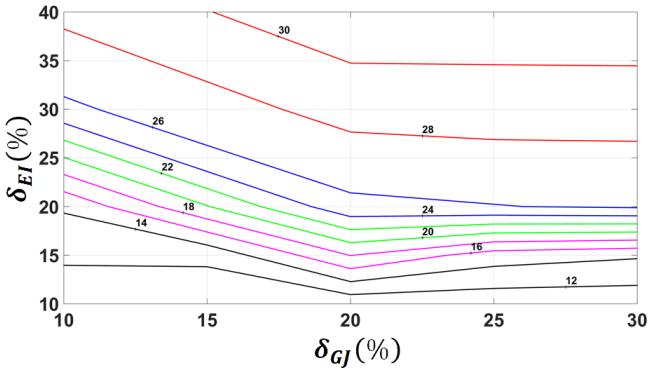

Fig. 8. Contour plot of blade tip twist (ϕ_{tip}) as a function of δ_{EI} and δ_{GJ}, evaluated at 100% NR.

and thickness ratio (e) together with chord-wise variation of fiber angle (θ) (but not span-wise), such that:

$$\begin{aligned} \underset{x}{\text{maximize}} \quad & \phi_{tip}(x) \\ \text{subject to} \quad & max\left(\left|\frac{EI-EI_0}{EI_0}\right|\right) \leq 0.4, \\ & max\left(\left|\frac{GJ-GJ_0}{GJ_0}\right|\right) \leq 0.4, \\ & ave\left(\left|\frac{EA-EA_0}{EA_0}\right|\right) \leq 0.4, \\ & r_i \leq 1, \end{aligned} \tag{6}$$

where $ave\,()$ denotes the relative difference of the average extensional stiffness of the new design with respect to the extension stiffness of the original UH-60A Black Hawk blade, as implemented in the RCAS model. The maximum variation in stiffness components is limited to 40% relative to the RCAS blade model. The material failure index is given by r_i, for $i = 1 \ldots N_e$, where N_e is the total number of elements of the finite element model of the UH-60A Black Hawk implemented in ABAQUS. Only centrifugal loading at 100%NR is considered in current optimization run. Furthermore, a 10% safety factor is embedded in the material failure index.

Starting from the design given in Figure 5, the design with the largest elastic, nose-down twist of 33° at 100%NR and 22° at 80%NR is given in Figure 9, where each color represents chord-wise variation of the design variables. This solution allows a change in elastic twist of up to 11° when the rotor speed is reduced by 20% (from 100%NR to 80%NR). With regards to Figure 9, this new design features large laminate thicknesses towards the root of the blade, with a sudden drop in thickness starting around 20% of the blade span and a slight increase in thickness for laminates along the leading and trailing edges starting around 70% of the blade span. Furthermore, the final design consists primarily of off-axis fibers and thickness ratios (e) approaching the maximum value of 0.9 outboard of 20% span for laminates within the blade leading edge and spar caps. The thickness of the off-axis fibers for the laminates along the trailing edge of the blade and the shear webs is close to 0.9 between $20\% - 60\%$ of the blade span and tapers off towards the blade tip. Finally, the angles of the off-axis fibers for the laminates along the leading edge and spar caps are 24° and 22° respectively while a higher angle of 42° is observed for the for fibers along the trailing edge of the blade. For the shear webs, the fiber angle is $-43°$.

The beam stiffness properties corresponding to the design solution in Figure 9 are shown in Figure 10. The trend in the beam stiffness of the new design, depicted in Figure 10, compares well against the RCAS reference stiffness properties, with the maximum difference in relative torsional, flap-wise bending stiffness being 37% and 39% respectively, while the relative difference in the average extensional stiffness around 40% with respect to the RCAS model. This indicates that the constraint on the stiffness components is active during the optimization, instead of the constraints on material strength, which are less that one as shown in Figure 11. The new design features larger lag-wise stiffness, compared to the baseline. However, this should not negatively affect the aeroelastic response of the new design since the new design is stiffer in lag-wise bending direction compared to the original RCAS design. The large laminate thickness close to the blade root corresponds with the increase in beam stiffness components toward the root section. Furthermore, the fact that the design solution is relatively constant between $20 - 60\%$ of the blade span also matches the constant beam stiffness in the same region, with slight reduction in GJ and flap-wise EI compared to corresponding RCAS blade stiffness components. The slight increase in the leading edge and spar cap laminates for the outer 30% of the blade span results in small increase of GJ and flap-wise EI over the same region.

Figure 11 shows the material failure index for the design solution for an elastic nose-down twist of 33° and centrifugal load evaluated at 100%NR. Failure indices exceeding one indicate material failure. As shown in Figure 11, the largest failure index is around 0.6, which conveys that no material failure occurs for the current design under centrifugal load at 100%NR. Furthermore, large values for the failure index are observed between $20 - 60\%$ of blade span, which corresponds with low laminate thickness and large thickness ratio over the same region. This means that laminates between $20 - 60\%$ of blade span are thin and comprised mostly of off-axis fibers that are not aligned with the beam axis, thus being less capable of supporting stresses along the beam axis. Further increases in extensional stresses, which could be potentially induced by aerodynamic bending moments could result in material failure over this same region.

MAXIMIZE ELASTIC TWIST UNDER CENTRIFUGAL & AERODYNAMIC LOAD IN HOVER

As mentioned in the previous section, the design that considers solely centrifugal load will most likely fail under material constraints when aerodynamic loads are superposed with the centrifugal load. Therefore, a new set of optimizations are carried out to maximize the elastic twist under centrifugal load at 100%NR and aerodynamic loads in hover, applied as frozen

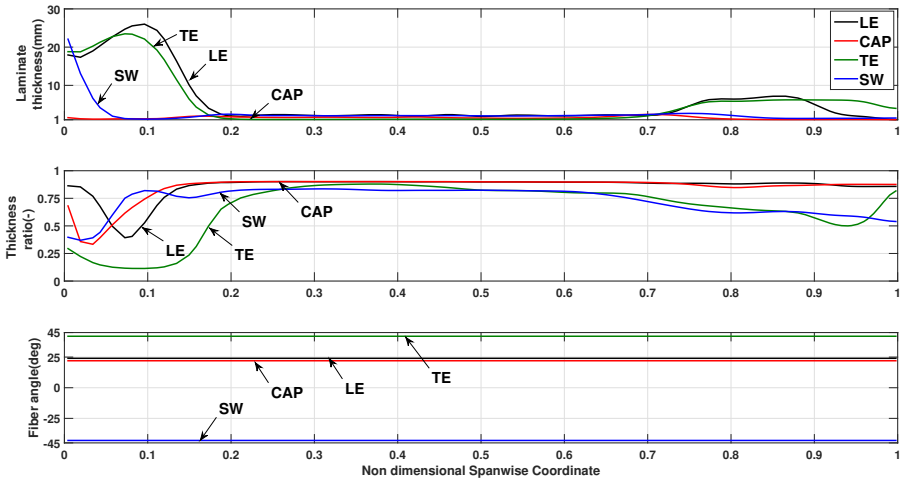

Fig. 9. Design solution for elastic tip twist of 33° at @100%NR considering only centrifugal load.

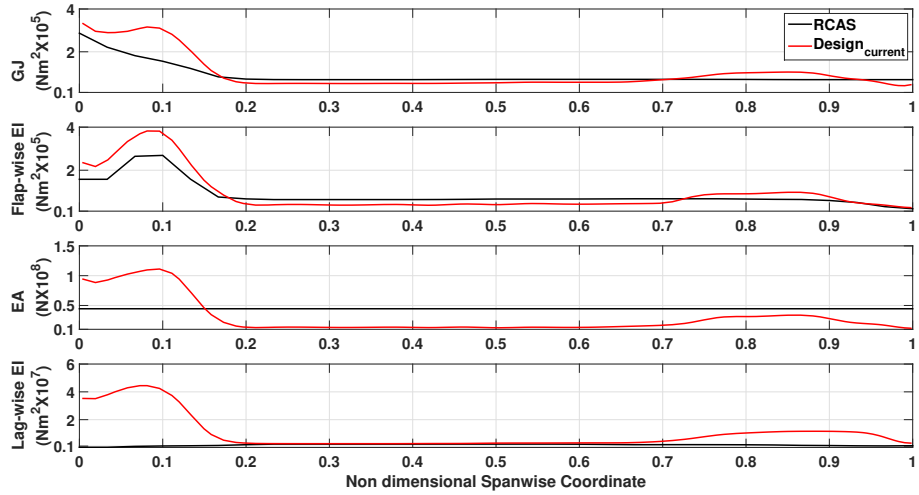

Fig. 10. Blade stiffness for elastic tip twist of 33° at @100%NR considering only centrifugal load.

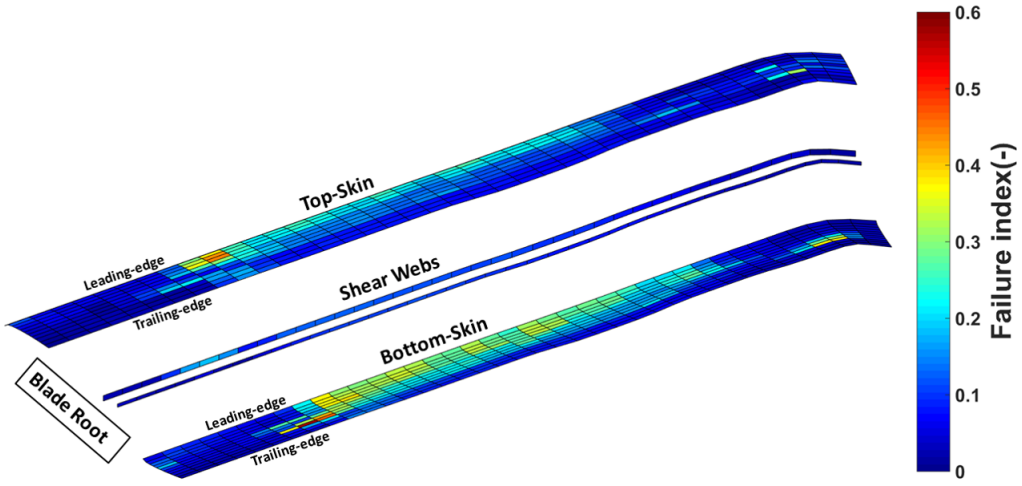

Fig. 11. Material failure index for elastic tip twist of 33° at @100%NR considering only centrifugal load.

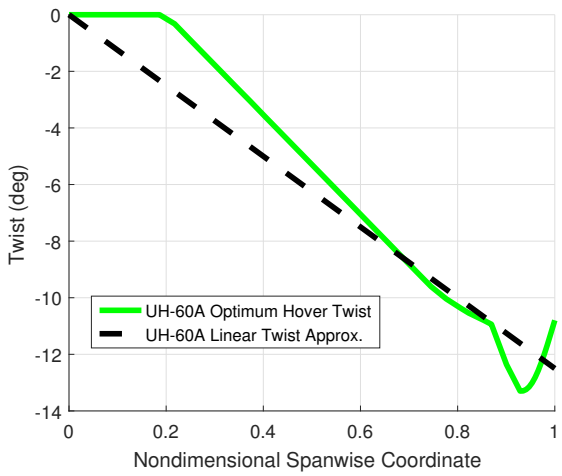

Fig. 12. Twist distribution comparison for the UH-60A blade.

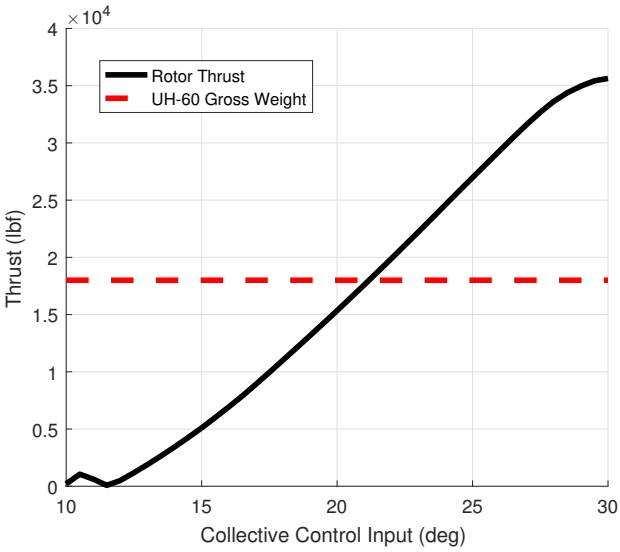

Fig. 13. Rotor thrust vs collective for the linearly twisted UH-60A blade.

loads, taken from a set of aeroelastic simulations in RCAS. The aircraft modeled in RCAS was a standard UH-60A Black Hawk with a gross weight of 18,000 lbs and zero shaft tilt. Thirteen typical nonlinear beam elements were used to structurally model the 26.83-foot blade span. A 12x12 Peters-He dynamic inflow model is used to compute the aerodynamic forces. The stiffness properties assigned to the blade were the diagonal terms from the fully populated composite stiffness matrix, which are the dominant contributors to the blade deflection under aerodynamic and centrifugal loads and also are the greatest in value by several orders of magnitude. The twisting effect of the extension-twist coupling term was mimicked by imposing the expected elastic twist (resulting from extension-twist coupling, or ETC) as built-in structural twist. That is, a 0° root pitch setting and a negative 12.5° linear twist distribution was imposed for both the aerodynamic and structural model within RCAS for the hover regime, which is an idealized linear expression of the actual nonlinear distribution, depicted as the dashed line corresponding to 100%NR in Figure 12. The other blade properties, namely the chord distribution, sweep distribution, airfoil distribution, and other geometric and spatial characteristics were not altered from the true UH-60A design.

The frozen aerodynamic loadings were computed using the stiffness properties of the original UH-60A blade, as described in the RCAS model, using a negative 12.5 degree linear twist distribution instead of the actual nonlinear twist. In the hover condition, the rotor collective control was trimmed to simply counteract the weight of the aircraft. Figure 13 depicts the rotor thrust as a function of the collective control input for the linearly twisted UH-60A blade. The rotor produces the amount of thrust required in hover at a collective root pitch control input of 21.2°, which corresponds to a root pitch setting of 21.2° and a tip pitch setting of 8.7°. A platform compounded with a wing and auxiliary propulsion would be heavier and could require a higher collective, per the figure. The aerodynamic forces and moments along the blade span for both the linearly and nonlinearly twisted UH-60A blades are shown in Figure 14, rotated into the reference frame of the blade root. There are close accordances in the sectional lift, drag, and pitch moment between the two blades, with the primary disparities outboard of 80% span, where the significant nonlinearity of the structural twist distribution in the original UH-60A blade geometry is present.

The aerodynamic loads associated with the model and parameters previously described are applied as static loads in the nonlinear beam optimization scheme. The current set of optimization runs do not consider constraints on the beam stiffness components. Furthermore, the shell elements of the finite element model of the blade corresponding to the blade root (the first 10% of the blade span) are also omitted since the root section will most likely be a solid section, such that the optimization is formulated as:

$$\begin{aligned} \underset{x}{\text{maximize}} \quad & \phi_{tip}(x) \\ \text{subject to} \quad & r_i \leq 1, \end{aligned} \tag{7}$$

where r is a material failure index of the active elements, which is multiplied by a safety factor of 1.1. The first five control points that affect the root section of the blade are constrained to vary with the same amount, reducing the total number of design variables to 180.

Starting from the blade design in Figure 9, the optimum design with the highest elastic nose-down twist of 25° at 100%NR and 16° at 80%NR is given in Figure 15, where each color represents chord-wise variation of the design variables. This design allows a total change in elastic twist of up to 25° between 0%NR and 100%NR. This corresponds to 9° when the rotor speed is reduced by 20% (from 100%NR to 80%NR). Referring to Figure 15, the optimizer tends to increase the thickness of the laminates belonging to the leading edge and spar caps, especially towards the root where a the laminate thickness is roughly 10mm. The spar cap and leading edge laminate thickness tends to decrease towards the

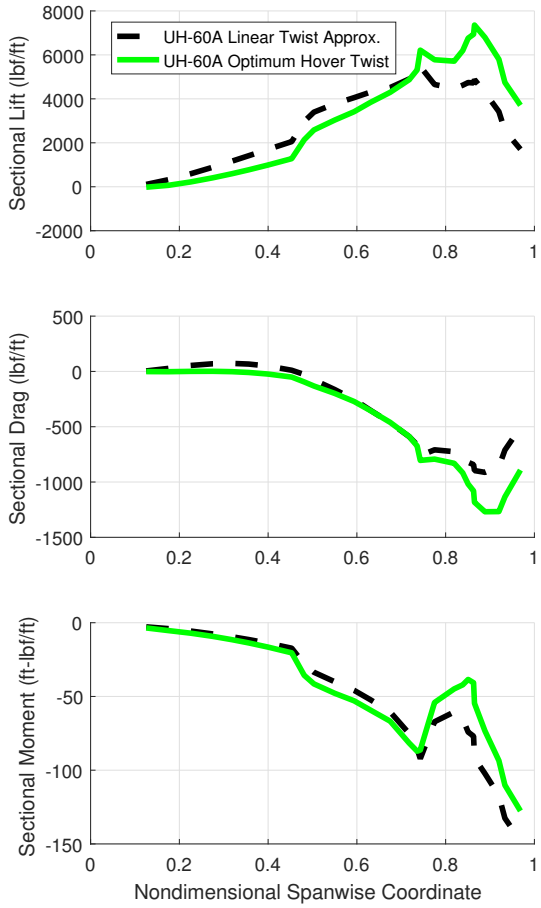

Fig. 14. Blade sectional forces and moments in hover.

blade tip such that 80% of the blade span and onwards, the thickness of all the laminates is around 1*mm*. The laminates belonging to the trailing edge, and shear webs all have small thickness, in order to reduce the torsional stiffness to maximize the elastic twist for a given extensional load. particularly the trailing edge laminate thickness is 1*mm* across the blade span, allowing for large elastic twist while considering material strength constraints (see Figure 17). Furthermore, all the laminates have large thickness ratio close to 90% across the blade span, suggesting a large fraction of the laminates consist of the off axis fibers. However, the thickness ratio of the trailing edge laminates drops slightly towards the blade root and blade tip, while for the shear webs a significant reduction in thickness ratio is observed between $10-40\%$ of blade span and slight reduction towards the blade tip, most likely done by the optimizer in order to increase the local membrane stiffness to comply with the strength constraint.

The angles of the off-axis fibers for the laminates along the leading edge and spar caps are 32° and 28° respectively, while the angle of fibers along the trailing edge has increased to 90° compared to the previous design shown in Figure 15. For the shear webs, the off-axis fiber angle remains at -43°.

The design solution given in Figure 15 is under the assumption of only in-plane loading condition, i.e. out-of-plane stress caused by pressure distribution across the blade surface is not taken into account. This gives the optimizer the freedom to only focus on the membrane stiffness of the laminates while ignoring bending stiffness consideration, i.e. reduce the laminate thickness as much as possible without breaching the material strength constraint in order to maximize the elastic twist.

The beam stiffness properties corresponding to the design of Figure 15 are shown in Figure 16. The torsional, flap-wise, and lag-wise bending stiffness components of the current design are greater for the first half of the blade and less towards the blade tip when compared against the RCAS reference stiffness properties. However, the extensional beam stiffness is smaller that the RCAS design throughout the blade radius. The average difference in torsional, flap-wise and lag-wise bending stiffness, and extensional stiffness are respectively 94%, 73%, 98% and 53%, with respect to the RCAS model of the UH-60A Black Hawk blade. This large decrease in extensional stiffness can be attributed to an attempt by the optimizer to maximize the elastic twist without violating the material failure constraints.

Finally, Figure 17 shows the material failure index for the design yielding an elastic, nose-down, twist of 25° under centrifugal load evaluated at 100%NR together with the aerodynamic load in hover. The largest failure index approaches 1 indicating that, while the current design is fully-stressed, there is no material failure under a combination of centrifugal and hover aerodynamic loads. Furthermore, the highest values for the failure index are observed at the bottom skin inboard of 80% of blade span. It can be noted that the large values of the failure index being on one side of the blade is the result of the additional flap-wise bending moment generated by the aerodynamic loads. This moment induces extensional stresses at the bottom skin while causing compressive stresses at the top skin. Therefore, the total stress, which is a combination of aerodynamic and centrifugal loads, increases in the bottom skin while decreasing in the top skin. Furthermore, Figure 17 indicates that the shear webs are also fully stressed, which is the result of large value for the thickness ratio and small laminate thickness across the blade span, resulting in reduced membrane stiffness of the shear web laminates.

The spin-up twist distributions at varying rotational rates for this 25° ETC design are depicted in Figure 18. Because the idealized linear twist distribution at hover is the same for the 25° ETC design as for the linearly twisted UH-60A blade design, the aerodynamic loadings should be quite similar. The aerodynamic loadings of both designs, as well as the nonlinearly twisted UH-60A blade, are shown in Figure 19. As the load and stiffness distributions are very close, the collective control input at which the rotor produces enough thrust to counteract the 18,000 lbs UH-60A gross weight is also very close, or 21.1° (see Figure 13). It is also important to note that because the aerodynamic forces affecting the linearly twisted UH-60A blade and the 25° ETC blade designs are so similar, a high level of confidence can be placed in the 'frozen-load' methodology implemented for this optimization scheme.

A comparison in several aeroelastic performance metrics is

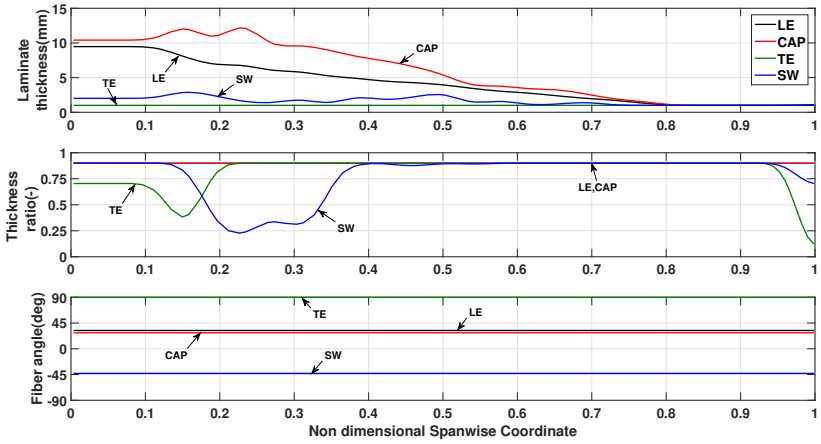

Fig. 15. Design solution for elastic tip twist of 25° at @100%NR considering both centrifugal and Aerodynamic load in hover.

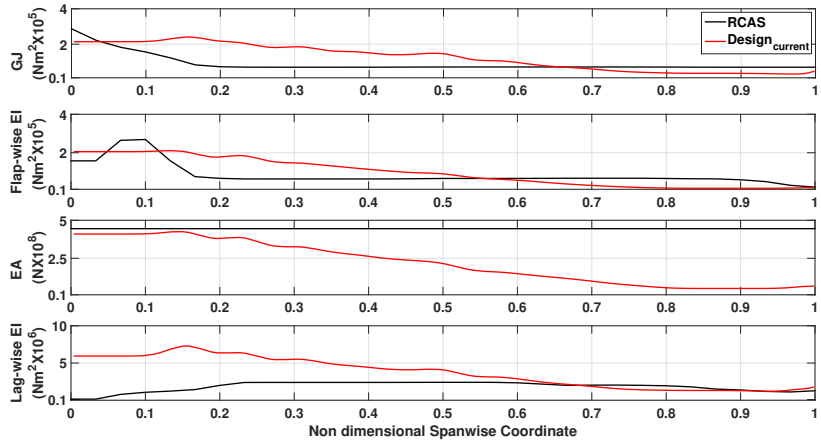

Fig. 16. Blade stiffness for elastic tip twist of 25° at @100%NR considering both centrifugal and Aerodynamic load in hover.

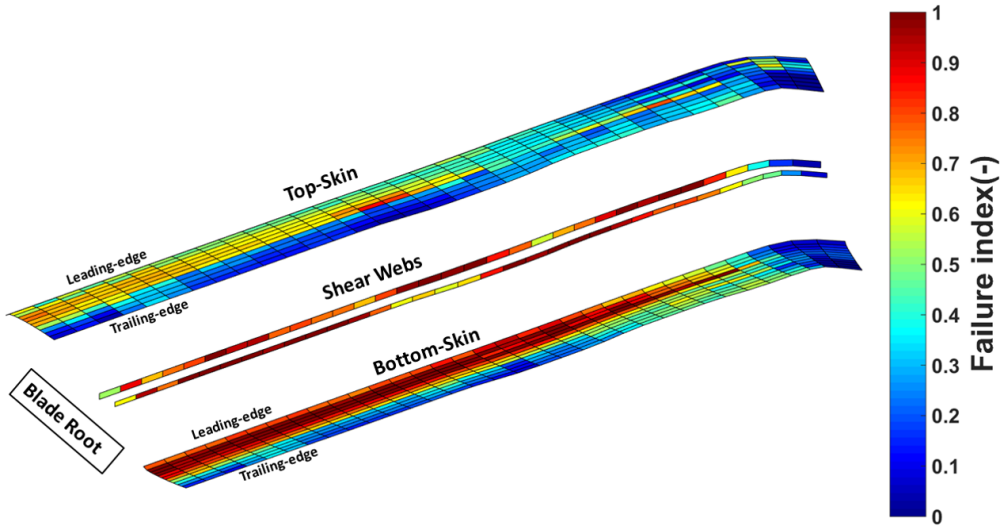

Fig. 17. Material failure index for elastic tip twist of 25° at @100%NR considering both centrifugal and Aerodynamic load in hover.

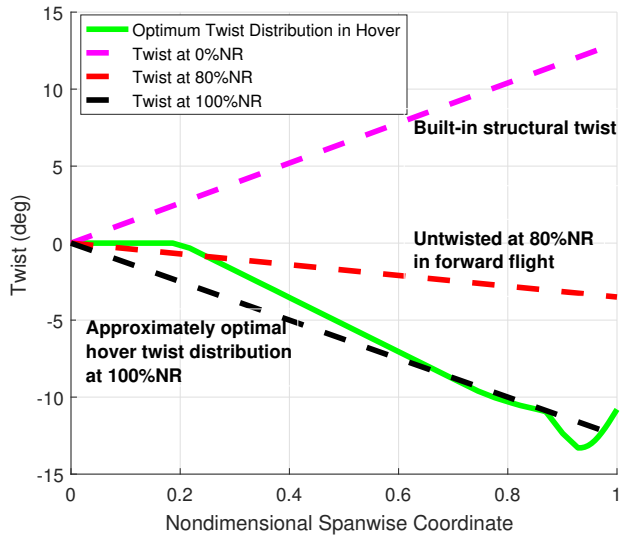

Fig. 18. Twist distributions for the 25° ETC blade.

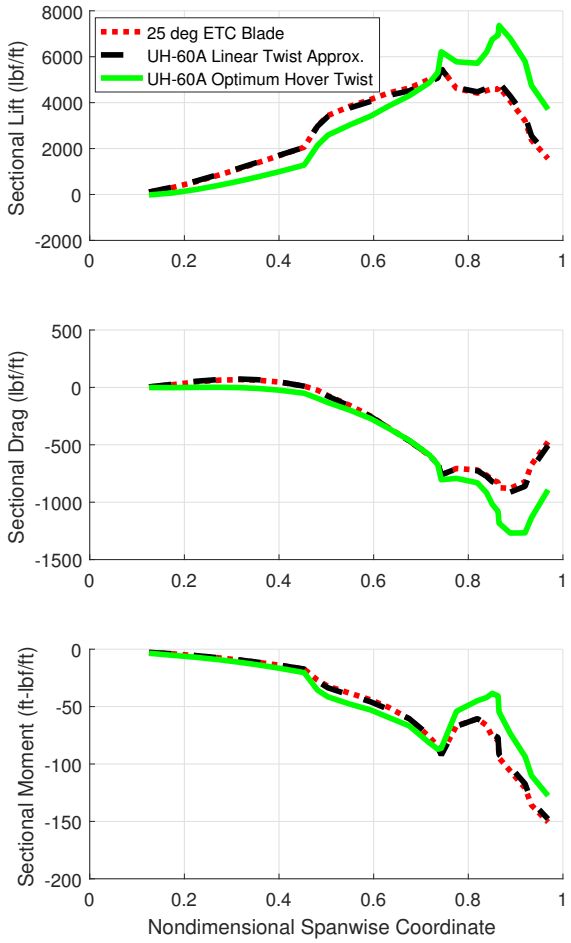

Fig. 19. Blade sectional forces and moments in hover.

Table 3. Hover performance comparison for UH-60A and 25° ETC blade.

Metric	Standard UH-60A Blade	25° ETC Blade
Trimming Collective (deg)	22.5	21.1
Coning Angle (deg)	3.1	3.2
Longitudinal Flapping (deg)	0.0	0.0
Lateral Flapping (deg)	0.0	0.0
Thrust (lbf)	18,000	18,000
Shaft Power (HP)	1920	1935

drawn between the standard UH-60A blade and the 25° ETC blade in Table 3 for the hover regime at 100%NR. The standard UH-60A blade is the original design of the Black Hawk blade, while the 25° ETC blade features the stiffness properties depicted in Figure 15 and the -12.5° linear twist depicted in Figure 18 at 100%NR. Despite the simplifying assumptions made, there is very close accordance between the performance characteristics of the two designs. The coning angles are quite similar and neither rotor experiences any 1/rev flap response. The 15 HP (1%) difference in the shaft power required to produce 18,000 lbs of vertical thrust can be attributed to the fact that the original UH-60A blade features nonlinear twist, which certainly has been optimized for hover performance, whereas the present composite design assumes a linear twist distribution. It is also noted that the supplemental nose-down twist induced by aerodynamic effects on the 25° ETC blade amounts to 1.96°, which is comparable to the 1-2° expected value for the standard UH-60A blade design.

CONCLUSION

This paper investigates the extension-twist coupling capability of composite rotor blades to passively vary the elastic twist distribution as a function of the rotational speed of the rotor. To this end, a framework is presented for optimizing extension-torsion coupled composite blades derived from the UH-60A Black Hawk. A composite laminate optimization method features the following design variables: laminate thickness, off-axis fiber angle, and thickness ratio of the off-axis fiber with respect to the total laminate thickness. The laminate thickness and ratio of the off-axis fibers vary both in the chord-wise and span-wise directions while the off-axis fiber angles vary only in the chord-wise direction.

The results show that a large change in tip twist as a function of rotational speed can be achieved using composite laminates while complying with material strength constraints under both centrifugal and aerodynamic loads in hover:

- It is demonstrated that an optimum blade can be designed to maximize the elastic twist while ensuring no material failure occurs for a blade rotating in a vacuum. Furthermore, the design was constrained such that the difference in beam stiffness of the optimum design, with respect to the beam stiffness of the RCAS model of the UH-60A blade, does not exceed 40%. For the optimum design, a change in tip twist of up to 11° is achieved by reducing the rotor speed by 20% (from 100%NR to 80%NR). However, this design does not guarantee tolerance of ma-

terial failure constraints if aerodynamic loads are considered.

- A new design is proposed that considers both centrifugal and aerodynamic loads in hover while accommodating material failure constraints. For this design, a change in tip twist of up to 9° is achieved by reducing the rotor speed by 20% (from 100%NR to 80%NR). The optimized blade performs closely to the original UH-60A blade in the hover flight regime at 100%NR.

- Chord-wise variation (and not span-wise variation) of the off-axis fiber angles seems to be sufficient in inducing substantial elastic twist under centrifugal loads like those experienced by present-day helicopters. Leading edge and spar cap sections of the blade seem to favor fiber angles around 30°, while for the trailing edge and shear web laminates, fiber angles around 90° and $-45°$, respectively, result in large elastic twist while adhering to material failure constraints.

- One possible implementation of the current design is a blade with linear (built-in) structural twist, varying from 0° at the root to 13° at the tip. When the rotor is spun up at 100%NR (for hover), the blade elastically twists to closely match a near-optimum linear twist distribution of $-12.5°$. When the rotor speed is reduced to 80%NR to accommodate compressibility effects on the advancing blade in high-speed forward flight, the blade will elastically untwist to only $-3.5°$ of linear tip twist along the blade span. This adaptivity could passively improve a wide range of rotor performance metrics in both regimes.

- The design is obtained under the assumption of only in-plane loading condition, i.e. out-of-plane stress caused by pressure distribution across the blade surface is not taken into account. This gives the optimizer the freedom to only focus on the membrane stiffness of the laminates while ignoring bending stiffness consideration, i.e. reduce the laminate thickness as much as possible without breaching the material strength constraint in order to maximize the elastic twist.

- Future work will implement necessary modifications to the blade design to accommodate exact span-wise and chord-wise pressure distributions of the aerodynamic loading in hover and forward flight. Furthermore, possible modifications to the proposed design will consider expanded failure modes of composite laminates, such as delamination.

REFERENCES

[1]Reddinger, J.-P., Gandhi, F., and Kang, H., "Performance and hub vibrations of an articulated slowed-rotor compound helicopter at high speeds," Proceedings of the 71st Annual American Helicopter Society Forum, Virginia Beach, Vol. 2, 01 2015.

[2]Keys, C., Tarzanin, F., and MacHugh, F., "Effect of twist on helicopter performance and vibratory loads," Proceedings of the 13th Annual European Rotorcraft Forum, Arles, France, 1987.

[3]Jacot, A. D. and Clingman, D. J., "Shape memory alloy consortium and demonstration," Smart Structures and Materials 2000: Industrial and Commercial Applications of Smart Structures Technologies, Vol. 3991, 2000.

[4]Ruggeri, R., Jacot, D., and Clingman, D., "Shape memory actuator systems and the use of thermoelectric modules," *Smart Structures and Materials*, 2002, pp. 386–394.

[5]Caldwell, N., Gutmark, E., and Ruggeri, R., "Performance Predictions of a Blade Twist Actuator System," 45th AIAA Aerospace Sciences Meeting and Exhibit, Vol. 8, 2007.

[6]Ruggeri, A. D., R. and Bussom, R., "Wind tunnel testing of a lightweight 1/4-scale actuator utilizing shape memory alloy," 49th AIAA/ASME/ASCE/AHS/ASC structures, structural dynamics, and materials conference, 2008.

[7]Mistry, M., Gandhi, F., Nagelsmit, M., and Gurdal, Z., "Actuation Requirements of a Warp-Induced Variable Twist Rotor Blade," *Journal of Intelligent Material Systems and Structures*, Vol. 22, (9), 2011, pp. 919–933.

[8]Prabhakar, T., Gandhi, F., Steiner, J., and McLaughlin, D., "A centrifugal force actuated variable span morphing helicopter rotor," ANNUAL FORUM PROCEEDINGS-AMERICAN HELICOPTER SOCIETY, Vol. 63, 2007.

[9]Moser, P., Barbarino, S., and Gandhi, F., "Helicopter Rotor-Blade Chord Extension Morphing Using a Centrifugally Actuated Von Mises Truss," *Journal of Aircraft*, Vol. 51, (5), 2014, pp. 1422–1431.

[10]Nixon, M. W., "Improvements to tilt rotor performance through passive blade twist control," *NASA Technical Memorandum 100583, Hampton, VA*, 1988.

[11]Lake, R. C., Nixon, M. W., Wilbur, M. L., Singleton, J. D., and Mirick, P. H., "A demonstration of passive blade twist control using extension-twist coupling," , 1992.

[12]Nixon, *Aeroelastic Response and stability of tiltrotors with elastically coupled composite rotor blades*, University of Maryland, 1993.

[13]Nampy, S. N., Smith, E. C., Shan, Y., and Bakis, C., "Extension-twist coupled tiltrotor blades using flexible matrix composites," Proc. 46th AIAA/ASME/ASCE/AHS/ASC Structures, Struct. Dynam. Mater. Conf. AIAA-2005, Amer. Inst. Aeronaut. Astronaut., Austin, Texas, 2005.

[14]Nampy, S. and Smith, E., "Design Evaluation of Model and Full-scale Flexible Matrix Composites Tiltrotor Blades with Extension-twist Coupling," AHS International 62nd Annual Forum, 2006.

[15]Ward, E. A., Chopra, I., and Datta, A., "RPM Driven Extension-Torsion Coupled Self-Twisting Rotor Blades," 27th International Conference on Adaptive Structures and Technologies, 2016.

[16]Ward, E. A., Chopra, I., and Datta, A., "RPM Driven Extension-Torsion Coupled Self-Twisting Rotor Blades," AHS International 73rd Annual Forum and Technology Display, 2017.

[17]Ward, E. A., Chopra, I., and Datta, A., "Design of Self-Twisting Rotor Blades for High-Speed Compound Rotorcraft," 25th AIAA/AHS Adaptive Structures Conference, 2017.

[18]Cottrell, J. A., Hughes, T. J., and Bazilevs, Y., *Isogeometric analysis: toward integration of CAD and FEA*, John Wiley & Sons, 2009.

[19]Ferede, E., *Static Aeroelastic Optimization of Composite Wind Turbine Blades using Variable Stiffness Laminates*, TU Delft, 2016.

[20]Ferede, E. A. and Abdalla, M. M., "Cross-sectional modelling of thin-walled composite beams," Proceedings of the 55th AIAA/ASMe/ASCE/AHS/SC Structures, Structural Dynamics, and Materials Conference, 2014.

[21]IJsselmuiden, S. T., *Optimal design of variable stiffness composite structures using lamination parameters*, TU Delft, 2011.

[22]Piegl, L. A. and Tiller, W., *The NURBS book*, Springer, 1995.